ACS APPLIED MATERIALS & INTERFACES

Forum Article

www.acsami.org

Effects of Nanoporous Carbon Derived from Microalgae and Its CoO Composite on Capacitance

Meng Zhou,[†] Joshua Catanach,[†] Joshua Gomez,[†] Stephanie Richins,[†] and Shuguang Deng*[,†,‡]

[†]Department of Chemical & Materials Engineering, New Mexico State University, Las Cruces, New Mexico 88003, United States

[‡]School for Engineering of Matter, Transport and Energy, Arizona State University, 551 East Tyler Mall, Tempe, Arizona 85287, United States

Supporting Information

ABSTRACT: Nanoporous carbon was synthesized from microalgae as a promising electrode material for electric double layer capacitors due to its large specific surface area and controllable pore structures. The pore textural properties of the algae-derived-carbon (ADC) samples were measured by N_2 adsorption and desorption at 77 K. The performance of the activated carbon (AC) as supercapacitor electrodes was determined by the cyclic voltammetry and galvanostatic charge/discharge tests. The effect of the nanoporous carbon structure on capacitance was demonstrated by calculating the contributions of micropores and mesopores toward capacitance. Capacitance was significantly affected by both pore size and pore depth. To further increase the specific capacity, a single-pot synthesis of porous carbon supported CoO composite (CoO/ADC) electrode material was developed using microalgae as the carbon source and $Co(OH)_2$ as both a carbon activation agent and CoO precursor. After carbonization, CoO particles were formed and embedded in the ADC matrix. The synergic contributions from the combined CoO and ADC resulted in better supercapacitor performance as compared to that of the pure CoO electrode. The calculated specific capacities of CoO/ADC were 387 and 189 C g^{-1} at 0.2 and 5 A g^{-1}, respectively, which were far more than the capacities of pure CoO electrode (185 C g^{-1} at 0.2 A g^{-1} and 77 C g^{-1} at 5 A g^{-1}). The cycle stability of CoO/ADC also increased significantly (83% retention of the initial capacity for CoO/ADC vs 63% for pure CoO). This research had developed a viable and promising solution for producing composite electrodes in a large quantity for commercial application.

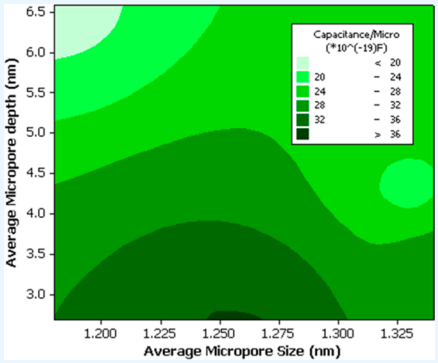

KEYWORDS: *microalgae, supercapacitor, pore depth, pore size, specific capacitance, specific capacity*

1. INTRODUCTION

Supercapacitors have several advantages over other energy storage devices, including high power density, fast charge−discharge rate, long life cycle, and environmental friendliness. They have extensive applications in hybrid cars, memory backup systems, and emergency systems in airplanes.[1−3] Recently, Tesla Motors announced its new model 3 battery cars with rapid acceleration (0−60 mph within 6 s) and short charging time;[4] these properties benefit from the outstanding power density of the supercapacitor. The synergetic contributions of batteries and supercapacitors make it possible to replace traditional fossil fuel completely with clean energy. However, unlike batteries, supercapacitors have low energy density.[5,6] Increasing energy density of supercapacitors without sacrificing other outstanding properties is crucial for enhancing the overall performances of supercapacitors.

Typically, supercapacitors can be divided into (1) electric double layer capacitors (EDLC) and (2) pseudocapacitors:

(1) For EDLC, the capacitance is from the electrostatic accumulation at the interfaces of the electrode and electrolyte. The surface area, pore size, and pore volume play important roles in EDLC.[7−11] The electrodes of EDLC are mainly made of carbon materials, such as activated carbon, carbon nanotubes, carbon sponge, graphene, et al.[12−21] The specific capacitance of EDLC is usually low (<400 F g^{-1}),[22] but both its thermal and chemical stability and conductivity are high. Carbon-based capacitors show low internal resistances, good rate capabilities, and long life cycles.[23−25] Among all carbon materials, activated carbon (AC) is one of the most extensively used electrode materials due to its good thermal and chemical stability, high conductivity, large specific surface area, controllable pore sizes, and low cost.[5,22] AC can be derived from biomass and agriculture waste, such as celtuce leaves, sugar cane, rice husks, sun flowers, peanut shells, et al.[26−31] AC has a wide range of pore sizes, covering micropore, mesopore, and macropore;[12,32] these nanopores within AC dictate the chemical and physical properties. The three pore sizes affect capacitance differently: micropores enhance the charge storage, mesopores increase the ion transportation and electron

Special Issue: New Materials and Approaches for Beyond Li-ion Batteries

Received: July 8, 2016
Accepted: September 16, 2016
Published: September 28, 2016

DOI: 10.1021/acsami.6b08328
ACS Appl. Mater. Interfaces 2017, 9, 4362−4373

Table 1. ADC Growth Condition, Pore Size, Surface Area, and Pore Volume

ADC	impregnate ratio	carbonization time (mins)	micro pore vol (cm^3/g)	micro pore surf area (cm^2/g)	meso pore vol (cm^3/g)	meso pore surf area (cm^2/g)	total pore vol (cm^3/g)	total pore surf area (cm^2/g)	micro pore surf area (%)	micropore vol (%)	mesopore surf area (%)	mesopore vol (%)
1	1	60	0.201	712.21	0.148	190.11	0.349	902.18	78.9	57.6	21.1	42.4
2	1	30	0.399	1304.53	0.280	278.01	0.678	1582.54	82.4	58.8	17.6	41.2
3	3	30	0.190	662.98	0.512	520.80	0.702	1183.78	56.0	27.1	44.0	72.9
4	3	60	0.228	810.61	0.588	595.28	0.817	1405.90	57.7	28.0	42.3	72.0
5	2	45	0.257	834.65	0.883	949.60	1.140	1784.25	46.8	22.6	53.2	77.4

conduction, and macropores work as electrolyte reservoirs.[33,34] Among the three types of pores, micropores are the main contributors to capacitances under low charge density. When the micropore sizes match the ionic sizes of the electrolyte, a maximum capacitance will be reached.[7,10,35] The optimal micropore size is about 0.7 and 0.8 nm for aqueous and organic electrolytes, respectively.[8,9] A single heuristic model established by Huang et al. explains how different types of pores affect the capacitance;[11] no more other explicit models were reported as far as we know.

(2) For the pseudocapacitors, the electrodes are mainly made of transition metal oxides; Faradaic reactions happen during the charge−discharge processes. The theoretical specific capacitances of pseudocapacitors are usually high (≥1000 F g^{-1}), but their real performances are poor, especially under high current densities. This can be attributed to low conductivity of metal oxides (except for RuO_2); agglomeration of particles, which reduces the interface and active sites for redox reactions; and strain accumulations during charge−discharge processes, which cause mechanical failure in the structures.[5,36−38]

Normally, the metal oxides cannot work separately as electrodes, instead they are usually combined with other conductive materials to serve as composite electrodes in capacitors. The conductive materials most widely investigated include carbon materials (previously discussed), copper foam, nickle foam, nanocone arrays, and titanium nanosheets.[39−47] The conductive materials work not only as a conducting network but also as a supporting matrix, which helps to disperse the metal oxide particles, increase the effective surface areas and the thermal and chemical stabilities, reduce the ion transfer resistances, release the strains, and further improve the capacitor's behavior.[22,48−51] However, the traditional methods to make such metal oxide composite electrodes are either tedious or very expensive. Activated nanoporous carbon is an ideal candidate to work as the supporting matrix[20,52,53] because of its easy synthesis, low cost, high surface area, comparably good conductivity, and easy combination with other materials. Recently, the design and preparation of nanoporous carbon materials have attracted great interests for supercapacitors, such as the designs of 3D porous carbon- and graphene-coated mesoporous carbon,[54,55] preparations of nanoporous carbons from folic acid, bimetallic MOF, and ZIF;[56−58] these carbons exhibited outstanding capacitor's properties.

In this work, AC was derived from waste algae. The effects of micropores on capacitance were studied by assuming that the pores had a cylindrical structure. Micropore depth was calculated from BET data. The pore depth was found to play an important role in the capacitance. In order to increase the capacity, $Co(OH)_2$ was used as an activation agent to derive AC from algae. The obtained CoO/ADC composite was used as an electrode in the supercapacitor directly without any further treatment. High capacities of 387 and 189 C g^{-1} were obtained at the current densities of 0.2 and 5 A g^{-1}, respectively, and 83% of the capacity retention was achieved after 5000 cycles at 3 A g^{-1}.

2. EXPERIMENTAL SECTION

2.1. Sample Preparation. *ADC Preparation.* Fresh microalgae samples (*Nanochloropsis salina* cultivated at New Mexico State University) were washed with deionized (DI) water under vacuum filtration, then dried in an oven at 80 °C for 24 h, and finally ground into fine powder. According to different impregnation ratios, a certain amount of microalgae powder and $ZnCl_2$ powder (anhydrous, 98%, from Alfa Aesar) were mixed by grinding. The powder mixture was dissolved in 500 mL of DI water, stirred, and heated at 140 °C in the silicon oil bath for 1 h, and dried in an oven at 60 °C for 24 h. Then the mixture was transferred into a tube furnace (Lindberg Blue M), heated at 550 °C with a heating rate of 1 °C min^{-1} in flowing nitrogen gas (ultrahigh purity, 99.99%, from Airgas) at the flow rate of 500 cm^3(STP) min^{-1} for 30−60 min, and finally cooled to the room temperature. The carbonized sample was refluxed with 3 M HCl (ACS 37%, from Acros Organics) at 70 °C for 1 h to remove Zn^{2+} and other residuals and then washed with DI water under vacuum filtration until the pH approached 7. The sample was dried in an oven at 60 °C for 24 h to obtain the ADC.

CoO/ADC Preparation. The mixture of dry algae (Nanochloropsis) with $Co(OH)_2$ (technical grade, 95%, Sigma-Aldrich) according to the impregnation ratio (wt %) of 1:5 in 200 mL of DI water was heated at 140 °C in a silicon oil bath until a slurry was formed. The slurry was moved to a crucible and transferred into a tube furnace (Lindberg Blue M), heated at 500 °C for 1 h with a heating rate of 1 °C min^{-1} under a nitrogen gas flow (flow rate, 500 cm^3(STP) min^{-1}). The obtained sample was used as the electrode without any further treatment.

2.2. Characterization. The ash content of ADC samples was determined by a PerkinElmer Pyris 1 thermogravimetric analyzer (TGA) in the temperature range of 25−900 °C at a heating rate of 10 °C min^{-1} with an air flow (10 mL/min).The crystal structure of the CoO/ADC composite was determined by powder X-ray diffraction (XRD, Rigaku Miniflex II) with Cu Kα radiation ($\lambda \approx 1.54$ Å). The surface morphology and microstructure were characterized with a transmission electron microscope (TEM JEOL-2010) and scanning electron microscope (SEM, Hitachi S-3400NII) with energy-dispersive X-ray spectroscopy (EDXS). The pore sizes, pore volumes, and size distribution were measured by nitrogen adsorption and desorption isotherms at 77 K using a Micromeritics ASAP2020 surface area and porosity analyzer. The conductivity was measured by atomic force microscope (AFM, Bruker Dimension Fastscan) with a conducting tip.

2.3. Electrochemical Test. The electrochemical performances were tested by galvanostatic charge/discharge cycling using a LAND CT2001A testing system at room temperature. The three electrode method was applied with 3 M KOH (99.98%, Alfa Aesar) as the electrolyte solution, Ag/AgCl as a reference electrode, and platinum foil as a counter electrode. For the working electrodes, 90 mg of ADC with 10 mg of polyvinylidene fluoride (PVDF) and 90 mg of CoO/ADC with 10 mg of PVDF were mixed in 5 mL of *N*-methyl-2-pyrrolidinone (NMP) separately, stirring for 12 h. The obtained slurries (2.6 mg of AC and 2.2 mg of CoO/AC) were coated uniformly on graphite substrates (1 cm × 1 cm) separately and then dried in a vacuum oven at 80 °C for 12 h to remove the solvent. Cyclic

DOI: 10.1021/acsami.6b08328
ACS Appl. Mater. Interfaces 2017, 9, 4362−4373

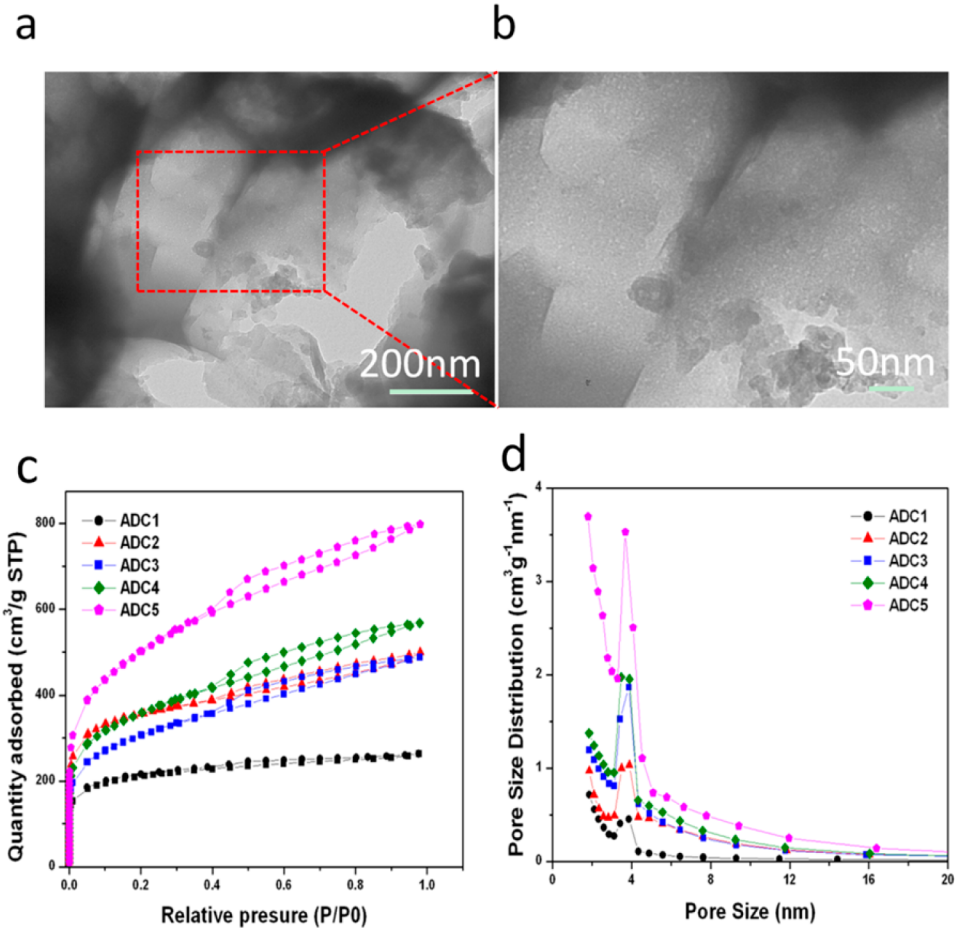

Figure 1. (a and b) TEM images of ADC pores; (c) N_2 adsorption and desorption isothermals at 77 K; (d) pore size distribution.

voltammetry (CV) curves were obtained using a VersaSTAT 4 employing the three electrode method mentioned above. Electrochemical impedance was studied using a CHI-680A (CH Instruments, Inc.) workstation.

Pure CoO (≥99.99%, trace metals basis, Sigma-Aldrich) was used as a control sample to study the ADC effects; the methods and assessments of pure CoO electrode were exactly the same as those for CoO/ADC.

3. RESULTS AND DISCUSSION

3.1. Pore Size, Specific Surface Area, and Pore Volume of ADC. Algae samples were activated by $ZnCl_2$ at 550 °C under different impregnation ratios (factor A) and different carbonization times (factor B). To optimize the experimental conditions, the experiments were designed according to 2^2 statistic factorial design with a middle point (Table 1). The specific surface area, pore volume, and the corresponding micropore and mesopore percentages measured from N_2 adsorption and desorption isothermals at 77 K were listed in Table 1. The residuals of ADC measured by TGA (Supporting Information Figure S1) were close to zero, which suggested a very low ash content in the final carbon samples. The porosities of the carbon surface were studied by TEM. Figure 1a shows the pores covering the whole surface of the AC, which enhanced the surface areas and pore volumes. The high porosity could increase the ion storage and transportation, and the well-formed network could work as fast lanes for electron conduction. Figure 1b shows varying pore sizes, and diverse pore size distribution. The relationship for specific surface areas, impregnation ratios, and carbonization time were shown in a cube (box) plot (Figure S2a) with a detailed explanation. The impregnation ratios had a bigger impact on performance than carbonization time (Figure S2b).

The nitrogen adsorption and desorption isotherms at 77 K were shown in Figure 1c. They were typically type IV isotherms with hysteresis loops within the relative pressure range 0.42−1 (P/P_0), which suggests that all the samples had well-developed mesopores. All the samples had wide ranges of pore size distribution from micropore (<2 nm) to mesopore (2−50 nm) (Figure 1d). The pore size distribution showed a peak at 3.8 nm, indicating that the pores were mainly in the region of large micropores and small mesopores. The samples had almost the same type of pore size distributions, which can be attributed to the effects of using the same activation agent and same activation temperatures.

3.2. Electrochemical Performance of ADC. The CV curves were measured at different scan rates ranging from 5 to 100 mV s^{-1}, as shown in Figure 2a (ADC1). At low scan rates (5, 10, and 20 mV s^{-1}), the curves were quasi-rectangular. At high scan rates (50 and 100 mV s^{-1}), the curves were highly distorted; the ions stored in the nanopores, especially in the micropores, could not respond to the high charge−discharge frequency change, which increased the diffusion resistances and reduced the capacitances.[59,60] At a low scan rate (5 mV s^{-1}), the CV curve shapes of all the samples (ADC1−ADC5) showed a slight difference (Figure 2b). However, at a high scan rate (100 mV s^{-1}; Figure 2c), the differences were very

DOI: 10.1021/acsami.6b08328
ACS Appl. Mater. Interfaces 2017, 9, 4362−4373

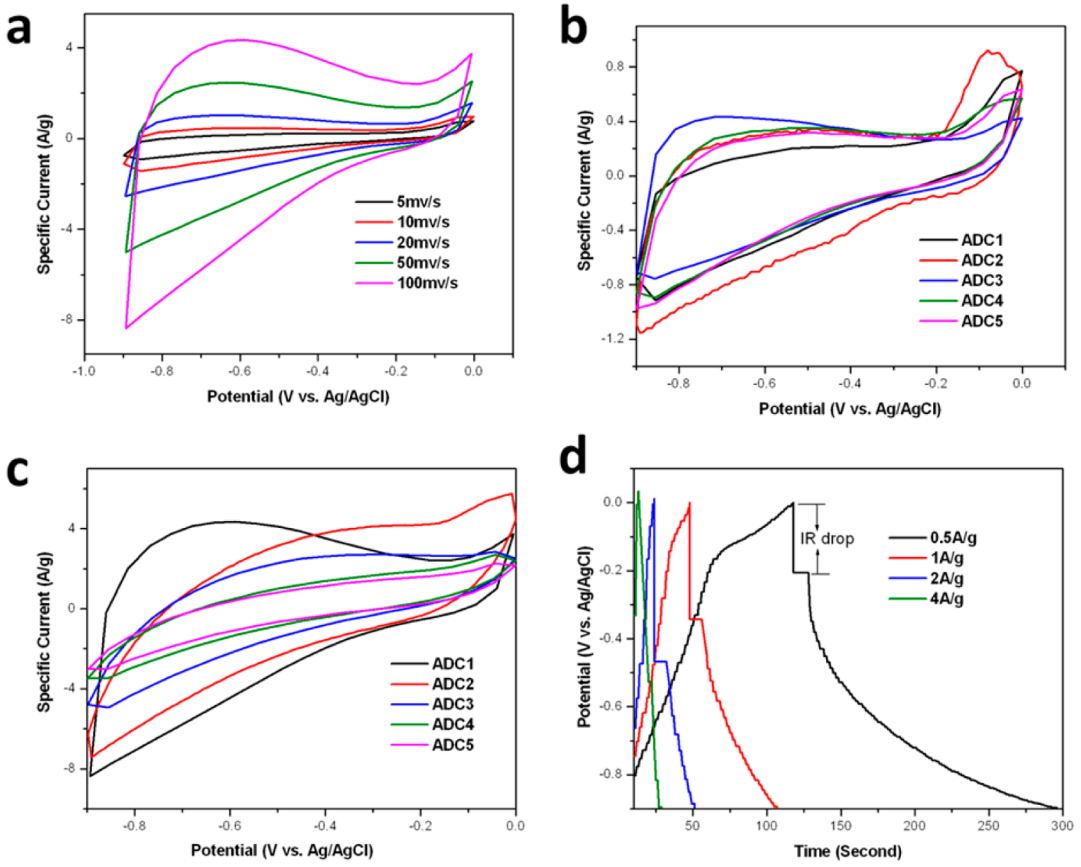

Figure 2. . (a) CV curve for ADC1 at different scan rates; (b) CV curve for all the samples at low scan rate (5 mV s^{-1}); (c) CV curve for all the samples at high scan rate (100 mV s^{-1}); (d) galvanostatic charge−discharge curves of ADC1.

significant, which may be attributed to the different concentrations of micropores and mesopores in each sample.

The galvanostatic charging−discharging tests were done at different current densities (0.5, 1, 2, and 4 A g^{-1}; Figure 2d, ADC1). The corresponding IR drops were 0.21, 0.34, 0.47, and 0.53 V, indicating the internal resistances increased with increasing current densities, which was consistent with the CV measurements. The nonlinear portions of the charge−discharge curves were caused by the near saturation of the ions in ADC, which might further hinder charge and discharge.[61]

The specific capacitances were calculated from the charge and discharge measurements using the following eq 1, where I is charge or discharge current, Δt is the discharge time after IR drop, m is the mass of the active material, and ΔV is the voltage window. The corresponding capacitances at different currents were shown in Table S1.

$$C = \frac{I\Delta t}{m\Delta V} \quad (1)$$

Different types of pores contribute differently to the capacitances: micropores could trap ions and increase the capacitance; however, this trapping also caused diffusion resistance and could become irreversible at high charge−discharge rates. Mesopores could provide fast ion transport channels, low ion diffusion resistances, and revisible storages (even at high rates). When the pore sizes matched the ion sizes, the micropores contributed to the capacitors, desolvating (partially desolvating) or distorting the solvated ions during the charging process. To fit the pore size, the distances between opposite charges were reduced, and the corresponding capacitance was increased.[8,10] During the discharging process, the resistances of ion diffusion through the pores increased due to such fitting, which eventually became irreversible at the high charge/discharge rates.

The ion diffusion time can be estimated from the formula $\tau = L^2/D$, where L is the diffusion distance for the diffusion inside pores (it is the length or depth of the pore) and D is the ion diffusion constant. At suitable pore sizes, the total charge amounts accumulating on the inner walls of pores were controlled by the diffusion time and equally determined by the depth of the pores. The deeper the pore was, the longer diffusion time was required. Under high charge and discharge rates, the allotted diffusion time might not be enough for ion transportation through the pores; only part of the pore could be used for charge accumulations.

In order to study the relationship between capacitance and pore depth, we assumed all the pores in the ADC were cylindrical, using the average pore sizes of micropore and mesopore for calculations. Combined with the data of specific surface areas and specific pore volumes listed in Table 1, we calculated the average depth (length) of micropores and mesopores as well as the specific numbers of micropores and mesopores (Table 2).

The rate capabilities (data in Table S1) were shown in Figure S3. To obtain the different activities of micropore and mesopore at different charging rates, the data were fitted exponentially (Figure S3). The results were shown in Table 3 with high R^2 values ($R^2 > 0.99$, where C is the capacitance and I is the applied current density). At high charge−discharge current densities (high frequencies), the ions' diffusion

DOI: 10.1021/acsami.6b08328
ACS Appl. Mater. Interfaces 2017, 9, 4362−4373

Table 2. Capacitance vs Pore Size and Depth

	av micropore size (nm)	av micropore depth (nm)	micropore no. ($\times 10^{19}$ g^{-1})	capacitance/micropore at 0.5 A g^{-1} ($\times 10^{-19}$)
ADC1	1.180	6.59	2.79	18.70
ADC2	1.340	3.49	8.10	29.10
ADC3	1.267	2.96	5.08	32.30
ADC4	1.260	2.68	6.85	38.00
ADC5	1.330	4.30	4.30	23.00

resistance increased in micropores and charge−discharge cycles became irreversible. When current density approached infinity, the contribution of the micropores to the capacitance reduced significantly. Meanwhile, mesopores had much better ion transportation and were less affected at high current densities; the contribution of the mesopores to capacitance did not change much with changing current density. On the other hand, surface function groups played important roles for the capacitances (pseudocapacitance). ADCs obtained at 550 °C had rich oxygen function groups[62] and the oxygen content could be detected by EDS (Figure S4b). Since all the functional groups were on the surface, the effects of ion diffusions on the pseudocapcitance did not change much with the changes of current density. In order to simplify the model and calculations, we treated the pseudocapacitance as a constant for each sample. To study the depth (length) factor of micropores at low charge rate, we further assumed that when current density (I) approached infinity, the micropores' contribution to capacitance was zero, all the capacitances were from mesopores and surface function groups. In this way, we were able to calculate the micropore capacitances at the low rate (for example, at 0.5 A g^{-1}) by subtracting the mesopore capacitances and pseudocapacitance from the total capacitances (Table 3), further divided by the total micropore numbers; then the capacitance of single micropore was calculated. The relationships of capacitance, pore size, and pore depth are shown in Table 2 and Figure 3. Relating capacitance to pore sizes (Figure 3a), the capacitance first increased with the increase of pore size, with a peak value at 1.25 nm, and then decreased with further size increasing which was consistent with the reported experimental results,[7,10] except for the peak position (0.7−0.8 nm from literature); this might be due to the our very simple model. Interestingly, we found that the single micropore capacitance decreased with the increase of pore depth (Figure 3b), which might be attributed to the following: (1) insufficient diffusion (only part of the pore depth could be used) and (2) when the charge−discharge was irreversible (the remaining ions could accumulate in the micropores, resulting in net charges which might screen other same charging ions). The combined effects of pore size and pore depth were shown in the contour plot (Figure 3c). The pore size and pore depth both played important roles in determining the capacitance. Micropores, which range from 1.18 to 1.34 nm displayed a high capacitance in low depth. The highest capacitance was observed when the pore size was very close to 1.25 nm with the depth lower than 3 nm. The capacitances of ADCs were comparable to the recently reported results, such as ACs derived from almond shells,[20] the cellulose-derived carbon,[30] and peanut-shell-derived carbon.[31]

3.3. Characterization of CoO/ADC. In order to increase the specific capacity, we derived a CoO/ADC battery type electrode using the single-pot carbonization method as mentioned above. Figure S4a shows the typical XRD pattern of the cubic phase CoO (JCPDS card no. 43-1004) with graphene (100) peak (JCPDS card no. 75-1621). The EDXS analysis further proved the existences of Co, O, C, Ca, Si, and S elements (residuals of algae) as shown in Figure S4b. The carbon content of the CoO/ADC sample from EDS measurement was around 12.4 wt %. SEM images in a variety of magnifications (Figure 4a,b) show that the sample was highly porous. The sponge-like structures of carbon not only worked as the supporting frames for CoO particles, the interconnections between pores also provided fast pathways for electron transfer. The large pores acted as reservoirs for the electrolyte, which helped reduce the ion diffusion distances and increase the interfaces between CoO particles and electrolyte. The nanopores (micropores and mesopores) could store the charges working as EDLC, which further enhanced the total capacitances.[5,63] The formation of these highly porous structures might be due to the high lipid contents in algae, which made pyrolysis easy at high temperatures, resulting in the sponge-like structures.[64] The BET surface area of CoO/AC was 121 m^2/g with pore volume 0.11 cm^3/g as shown in Figure S5.

Figure 5a shows the TEM images of CoO/ADC. CoO nanoparticles were better dispersed than pure CoO as shown in Figure 5b. The porous ADC matrix prevented agglomerations and extended the active sites for redox reactions. CoO particles were embedded in the carbon matrix (Figure 5c). The surrounding carbon (red area in Figure 5c and inset) formed the conducting network, improved the electron transports, and reduced the internal resistances. These conclusions could be further proved by AFM. Figure 5d shows the schematic drawing of the in situ tunneling current measurement. The Au-coated Si was used as conductive substrate, and the applied bias voltage was 5 V (DC). Figure 5e displays the 3D plot of the tunneling current measurement using the AFM peak force Tuna mode. The peak areas (pink and green) were the conducting areas (high currents), which were carbon for our case. The dark yellow areas were high-resistance areas (low currents), related to CoO particles. Figure 5f was the AFM adhesion force measurement. The higher the atomic mass is, the higher the forces between atoms and AFM tips are. The peak areas represented the CoO particles; the valley (red) areas showed the carbon and pores. The overlap between the conducting and heavy mass areas demonstrated that the CoO particles were

Table 3. Fitting of Current Density (A g^{-1}) vs Specific Capacitance (F g^{-1})

sample	fitting results	R^2 of fitting	capacitance (I at infinity) (F g^{-1})	total capacitance (I at 0.5 A g^{-1}) (F g^{-1})	micropore capacitance (I at 0.5 A g^{-1}) (F g^{-1})
ADC1	$C = 72.03354 + 277.44796 \exp(-I/0.29954)$	0.99997	72	124	52
ADC2	$C = 92.06233 + 1256.27965 \exp(-I/0.29895)$	0.99945	92	328	236
ADC3	$C = 30.25379 + 414.22265 \exp(-I/0.53848)$	0.99838	30	194	164
ADC4	$C = 30.02536 + 1082 \exp(-I/0.35038)$	0.99978	30	290	260
ADC5	$C = 16.86 + 264.84 \exp(-I/0.50891)$	1	17	116	99

DOI: 10.1021/acsami.6b08328
ACS Appl. Mater. Interfaces 2017, 9, 4362−4373

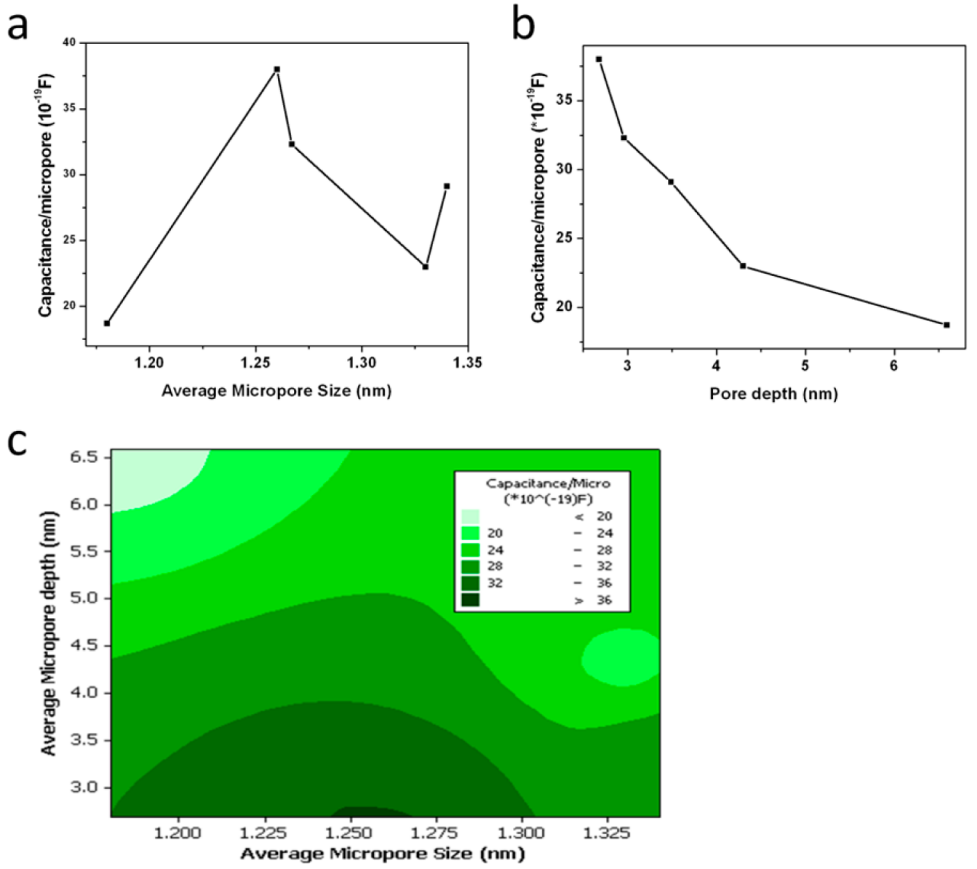

Figure 3. (a) capacitance vs pore size; (b) capacitance vs pore depth (length); (c) contour plot of capacitance, pore size, and depth.

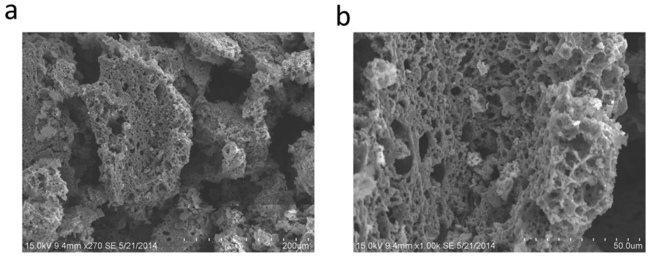

Figure 4. SEM of CoO/ADC at low (a) and high (b) magnifications.

covered by carbon, due to the pore collapses or thermal shrinks during the heat treatments.

3.4. Electrochemical Performance of CoO/ADC. The cyclic voltammetry curves shown in Figure 6a (CoO/ADC) and Figure 6b (pure CoO) had scan rates from 5 to 100 mV s^{-1}. Multiple redox broad peaks were observed, indicating that the Faradaic reactions of CoO were the main contributors to the overall capacities. The marked peaks in Figure 6c correspond to the oxidation of Co^{2+} to Co^{4+} (peaks a and a′) and reduction peaks Co^{4+} to Co^{3+} (peaks b and b′), Co^{3+} to Co^{2+} (peaks c and c′) at scan rate of 5 mV s^{-1}, which were typical battery type electrode behaviors.[65−67]

The possible reactions could be summarized as

$$CoO + 2OH^- = CoO_2 + H_2O + 2e^-$$

(oxidation, peaks a and a′)

$$CoO_2 + H_2O + e^- = CoOOH + OH^-$$

(reduction, peaks b and b′)

$$CoOOH + e^- = CoO + OH^-$$

(reduction, peaks c and c′)

Due to the high scan rate of 100 mV s^{-1}, there was an increase in reaction speed resulting in the reduction peaks c and c′ disappearing in Figure 6d.

The comparisons of CoO/ADC and CoO (Figure 6c,d,) indicate similar behaviors at both low scan rates (5 mV s^{-1}) and high scan rates (100 mV s^{-1}). The areas of CoO/ADC were larger than that of CoO from the CV curves. The larger integrated areas represented the higher specific capacitances. Although the theoretical capacitance of pure CoO (4292 F g^{-1}) is higher than that of CoO/ADC ($C_{\text{theor of CoO/ADC}} = C_{\text{carbon}} \times$ carbon% (wt) + $C_{\text{CoO}} \times$ CoO% (wt), assuming C_{carbon} is 200 F g^{-1}, 12.4% of carbon in CoO/ADC from EDS measurement, $C_{\text{theor of CoO/ADC}}$ = 3785 F g^{-1}).[22,36] This further proved the efficiency of CoO in ADC was higher than that of pure CoO, which could be attributed to the good dispersion of CoO particles in the ADC matrix, resulted in larger effective surface areas and more redox active sites between CoO particles and electrolytes.

The galvanostatic discharge curves were shown in Figure 7a with the applied current densities from 0.2 to 5 A g^{-1}; the corresponding specific capacities were calculated according to the following formula:

DOI: 10.1021/acsami.6b08328
ACS Appl. Mater. Interfaces 2017, 9, 4362−4373

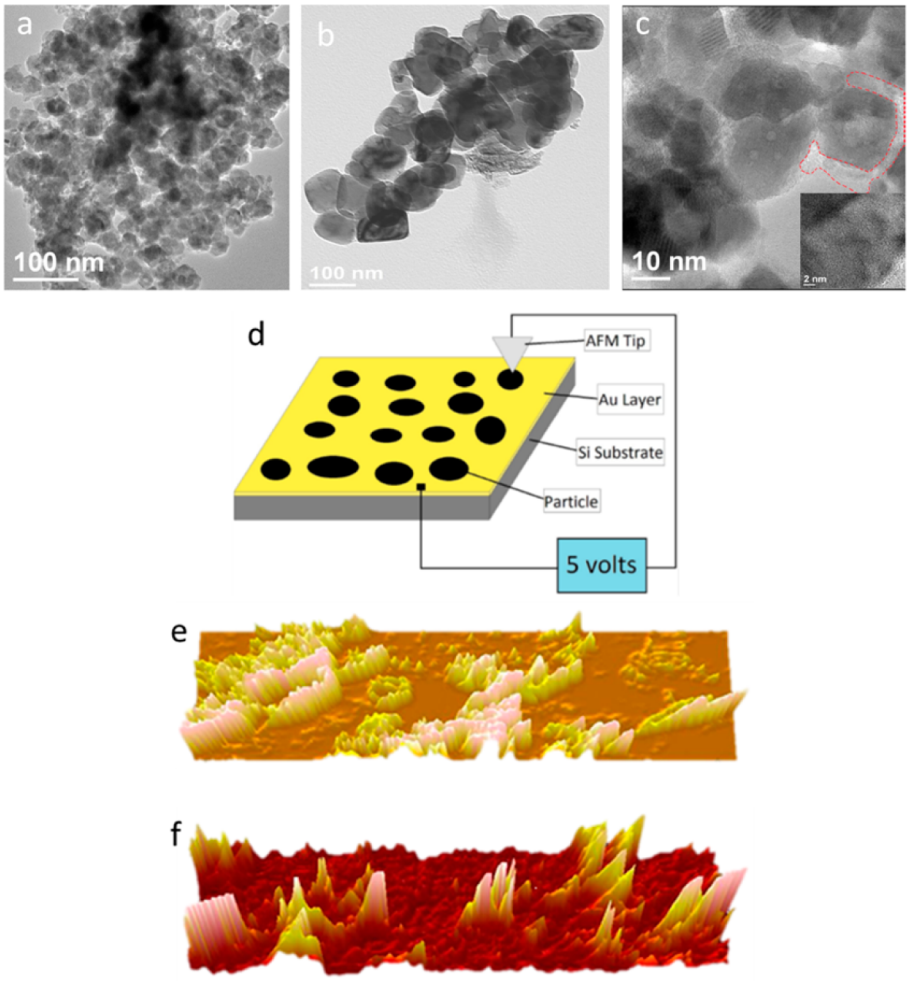

Figure 5. (a) Low magnification TEM image of CoO/ADC; (b) low magnification TEM image of pure CoO; (c) high magnification TEM image of CoO/ADC (inset: TEM image of the selected area); (d) schematic drawing of the tunneling current measurement; (e) AFM mapping of the tunneling current; (f) AFM mapping of adhesion force of CoO/ADC.

$$\text{specific capacity} = \frac{I}{m}\Delta t \tag{2}$$

where I/m is the applied current density and Δt is the discharge time.

The galvanostatic charge−discharge comparison of CoO/ADC and pure CoO at current density of 0.2 A g^{-1} was shown in Figure 7b. The discharge time of CoO/ADC was much longer than that of pure CoO; the specific capacity of CoO/ADC was much higher than CoO, which was consistent with the CV measurement. In addition, CoO/ADC had a more symmetric shape, which represents a better capacitor behavior. The calculated specific capacities of CoO/ADC and pure CoO were 387 and 185 C g^{-1} at 0.2 A g^{-1} (corresponding specific capacitances were 859 and 410 F g^{-1}, but it was more accurate to use C g^{-1} for the battery type electrode): the capacities were 189 and 77 C g^{-1} at 5 A g^{-1}, respectively (420 and 172 F g^{-1}). With the help of the ADC matrix, the specific capacity was doubled. The lowest measured capacity of CoO/ADC (189 C g^{-1} at 5 A g^{-1}) was still higher than the highest capacity of CoO (185 C g^{-1} at 0.2 A g^{-1}); therefore the ADC improved the electrodes. CoO/ADC electrode was also tested under larger current density, 10 and 20 A g^{-1} (inset of Figure 7a); the capacities of 156 and 133 C g^{-1} were obtained (347 and 296 F g^{-1}). Compared with the most recently published results, the capacitance of CoO/ADC was higher than 3D graphene (266 F g^{-1} at 0.5 A g^{-1}),[68] Co_3O_4/carbon (469 F g^{-1} at 1 A g^{-1}),[53] MnO_2/OCN/PVDF (414 F g^{-1} at 0.35 A g^{-1}),[69] FeMnO (243 F g^{-1} at 1 A g^{-1}),[70] and 3D TiO_2@RGO (397 F g^{-1} at 0.36 A g^{-1}).[71]

The rate capabilities were shown in Figure 7c. Both materials' capacitances decreased with the increase of current densities. The cycle stability (Figure 7d, inset was the normalized figure) was measured at a current density of 3 A g^{-1}. After 5000 cycles, 83% of the initial capacity remained for CoO/ADC, while it was 63% for CoO. Electrochemical impedance spectrum (EIS) was performed from 0.01 to 10^5 Hz with AC amplitude of 5 mV. Figure S6 shows that CoO/ADC had a steeper slope than that of CoO, which indicated a better capacitor behavior. The equivalent series resistance of CoO/ADC was 0.6 and 1.1 Ω for CoO, as shown in the inset of Figure S6.

The applications of ADC in the composite electrodes can be summarized as follows: (1) the ADC expanded the interfaces, increased active redox sites, and reduced agglomerations of particles; (2) the high conductivity carbon formed fast lanes for electron transportation, which reduced the internal resistances; (3) the large pores of ADC worked as reservoirs for electrolyte, which shortened the ion diffusion distances; (4) the high surface areas of ADC could work as EDLC, providing extra

DOI: 10.1021/acsami.6b08328
ACS Appl. Mater. Interfaces 2017, 9, 4362−4373

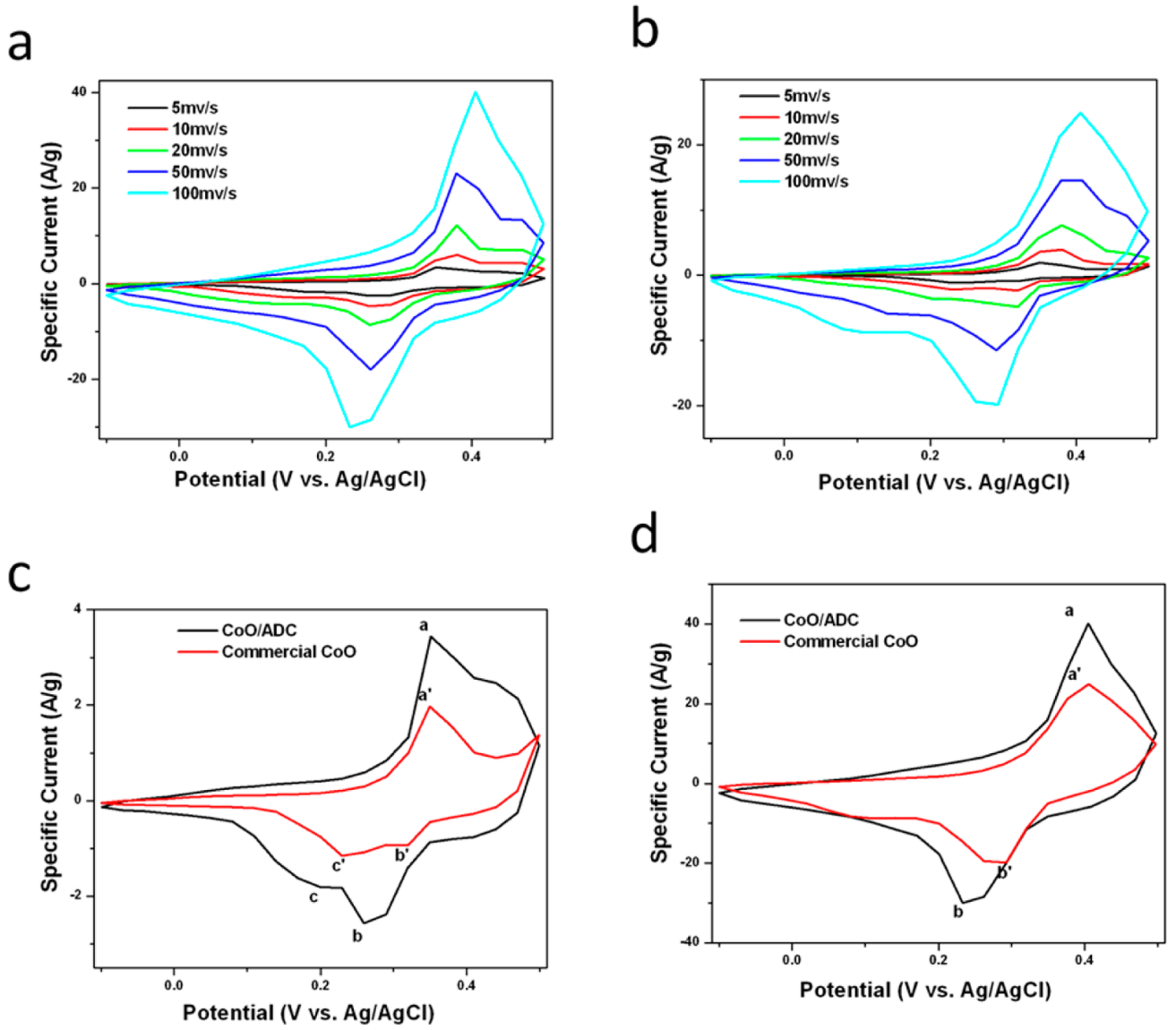

Figure 6. (a) CV curves of CoO/ADC at different scan rates; (b) CV curves of pure CoO; (c) CV curves of CoO/ADC and pure CoO @ 5 mV s^{-1}; (d) CV curves of CoO/ADC and pure CoO @ 100 mV s^{-1}.

capacitance; (5) the sponge structure of the ADC matrix worked as a buffer layer to release the strain that accumulated during the charge−discharge process to extend the cycle stabilities.

In order to test the practical application of CoO/ADC electrode, an asymmetric supercapacitor cell was built-up using CoO/ADC as the positive electrode (+) and ADC2 as the negative electrode (−), the mass balance was based on $Q_+ = Q_-$ ($m_+C_+V_+ = m_-C_-V_-$). The GCD curve was shown in Figure S7a, an energy density of 26.1W h/kg could be achieved at the power density of 337W/kg, the energy density was higher than those of the CuO//AC cell (19.7W h/kg),[72] Co_3O_4/MnO_2// MEGO cell (18 W h/kg),[73] $Ni(OH)_2$/GNs/NF//AC (11.1W h/kg),[74] and $NiCo_2O_4$−rGO//AC (23.32 W h/kg).[75] The cycle stability was measured at 1 A/g, after 1000 cycles, with 87% of the initial capacitance retained (Figure S7b).

The cost to make such an asymmetric cell was very low; the procedure was very simple, and it was possible to commercialize such a product. The Ragone plot comparing our work with the commercial energy storage device was shown in Figure S7c; our product showed better energy density than the commercial supercapapcitors.

4. CONCLUSIONS

Nanoporous carbon samples were derived from fresh microalgae at 550 °C with $ZnCl_2$ as the activation agent at different impregnation ratios and carbonization times. N_2 adsorption and desorption isotherms showed that ADCs had large surface areas and large pore volumes, which were mainly from micropores and mesopores. By assuming a cylindrical structure of all the pores, the average pore depth was calculated. Electrochemical measurements showed that both micropores and mesopores significantly contributed to the capacitance in the carbon electrodes. At low charge−discharge current density (0.5 A g^{-1}), the average capacitance from the micropores decreased with increasing pore depth, which was caused by a longer charge diffusion distance and net charge residuals. A peak capacitance was observed in the median pore size of 1.25 nm with short pore depth (<3 nm), which may be caused by the distortion of solvated ions under electric fields, and this

DOI: 10.1021/acsami.6b08328
ACS Appl. Mater. Interfaces 2017, 9, 4362−4373

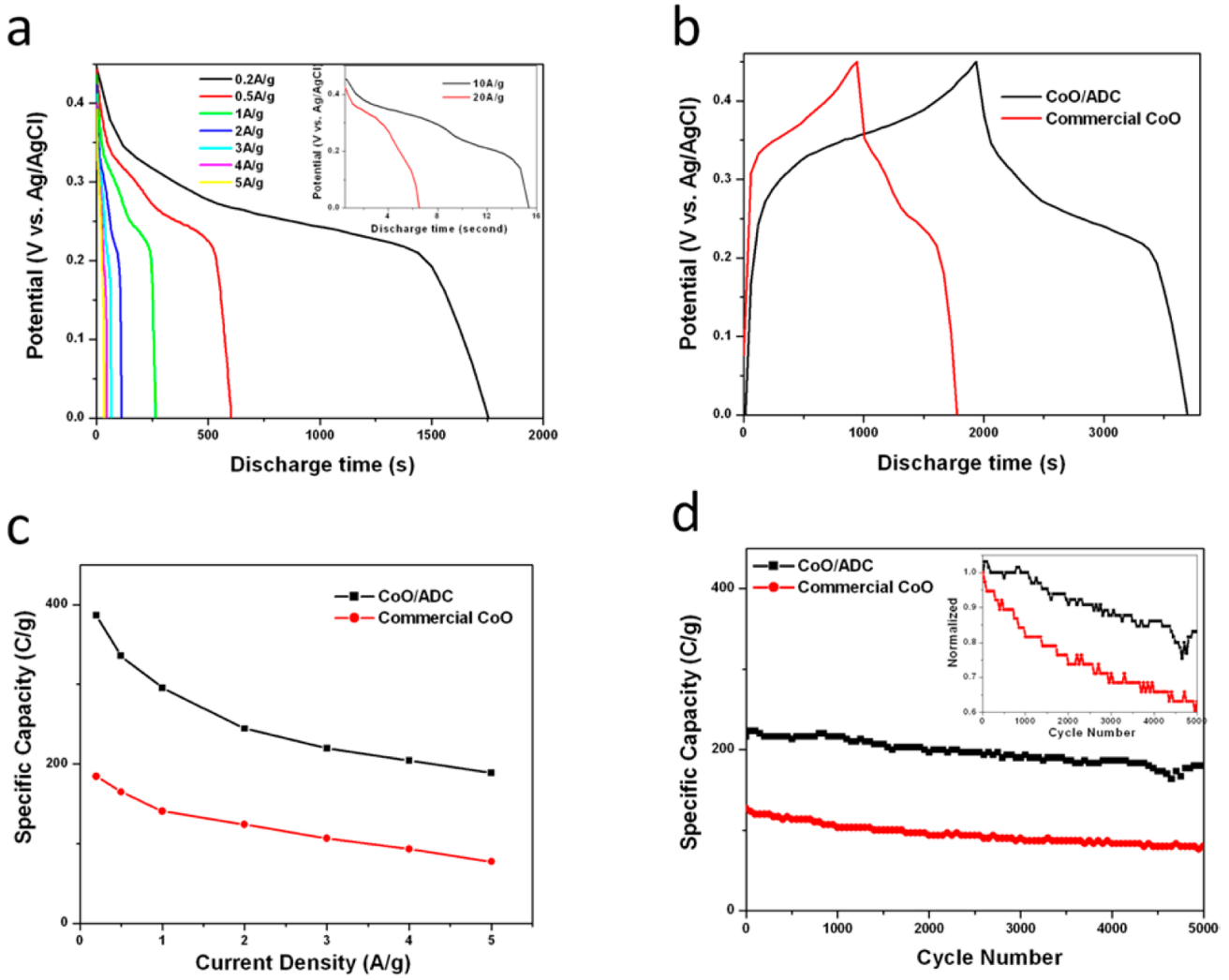

Figure 7. (a) Galvanostatic discharge curves for CoO/ADC (inset: current densities at 10 and 20 A g^{-1}); (b) galvanostatic charge−dischage curves of CoO/ADC and pure CoO at 0.2 A g^{-1}; (c) rate capability; (d) cycle stability (inset: normalized capacitance vs cycle number).

distortion was favorable for the close packing of solvated ions. To increase the specific capacity, a composite electrode consisting of CoO embedded in an ADC matrix was successfully synthesized using a single-pot method. The CoO/ADC composite electrode had achieved more than double the specific capacity of a pure CoO electrode. The ADC matrix played an important role in increasing the specific capacity and cycle stability, as well as reducing the internal resistances of the composite electrode. The significant improvements of the CoO/ADC composite electrode could be attributed to the high lipid content of algae, which enabled an easy carbonization, producing a loose and porous carbon structure that helped to increase the performance. Using this simple method, other metal oxide/ADC composite electrodes could be easily produced; it is also possible to make printable high-quality electrodes.

■ ASSOCIATED CONTENT

Supporting Information

The Supporting Information is available free of charge on the ACS Publications website at DOI: 10.1021/acsami.6b08328.

Figures showing TGA, factor box plot and Pareto chart including details of factorial analysis, rate capabilities and fittings, XRD, EDS, BET, EIS, discharge curves and cycle stability, and a Ragone plot and a table listing capacitances under different current densities (PDF)

■ AUTHOR INFORMATION

Corresponding Author

*Tel.: +1 4807277238. Fax: +1 4807279321. E-mail: shuguang.deng@asu.edu.

Notes

The authors declare no competing financial interest.

■ ACKNOWLEDGMENTS

This project was partially supported by the U.S. Department of Energy (Grant DE-EE0006316) and U.S. National Science Foundation (Grants EEC-1028968, MRI-1229558, and IIA-1301346). S.D. acknowledges the support from the Fulton Schools of Engineering at Arizona State University.

■ REFERENCES

(1) Ramadoss, A.; Kim, S. J. Improved Activity of a Graphene−TiO2 Hybrid Electrode in an Electrochemical Supercapacitor. *Carbon* **2013**, *63*, 434−445.

DOI: 10.1021/acsami.6b08328
ACS Appl. Mater. Interfaces 2017, 9, 4362−4373

(2) Winter, M.; Brodd, R. J. What are Batteries, Fuel Cells, and Supercapacitors? *Chem. Rev.* **2004**, *104*, 4245−4269.
(3) Zainal Abidin, H. E.; Hamzah, A. A.; Majlis, B. Y.; Yunas, J.; Abdul Hamid, N.; Abidin, U. Electrical Characteristics of Double Stacked Ppy-PVA Supercapacitor for Powering Biomedical MEMS Devices. *Microelectron. Eng.* **2013**, *111*, 374−378.
(4) Los Angeles Times. Elon Musk Says Tesla Model 3 Pre-orders Hit 180,000, But Can He Deliver? http://www.latimes.com/business/la-fi-elon-musk-tesla-model3-20160331-story.html (accessed Sep. 14, 2016).
(5) Zhi, M. J.; Xiang, C. C.; Li, J. T.; Li, M.; Wu, N. Q. Nanostructured Carbon-Metal Oxide Composite Electrodes for Supercapacitors: A Review. *Nanoscale* **2013**, *5*, 72−88.
(6) Ma, Y.; Chang, H.; Zhang, M.; Chen, Y. Graphene-Based Materials for Lithium-Ion Hybrid Supercapacitors. *Adv. Mater.* **2015**, *27*, 5296−5308.
(7) Largeot, C.; Portet, C.; Chmiola, J.; Taberna, P. L.; Gogotsi, Y.; Simon, P. Relation Between the Ion Size and Pore Size for an Electric Double-Layer Capacitor. *J. Am. Chem. Soc.* **2008**, *130*, 2730−2731.
(8) Raymundo-Pinero, E.; Kierzek, K.; Machnikowski, J.; Beguin, F. Relationship Between the Nanoporous Texture of Activated Carbons and Their Capacitance Properties in Different Electrolytes. *Carbon* **2006**, *44*, 2498−2507.
(9) Béguin, F.; Presser, V.; Balducci, A.; Frackowiak, E. Carbons and Electrolytes for Advanced Supercapacitors. *Adv. Mater.* **2014**, *26*, 2219−2251.
(10) Chmiola, J.; Yushin, G.; Gogotsi, Y.; Portet, C.; Simon, P.; Taberna, P. L. Anomalous Increase in Carbon Capacitance at Pore Sizes Less Than 1 Nanometer. *Science* **2006**, *313*, 1760−1763.
(11) Huang, J.; Sumpter, B. G.; Meunier, V. A Universal Model for Nanoporous Carbon Supercapacitors Applicable to Diverse Pore Regimes, Carbon Materials, and Electrolytes. *Chem. - Eur. J.* **2008**, *14*, 6614−6626.
(12) Wang, H.; Xu, Z. W.; Kohandehghan, A.; Li, Z.; Cui, K.; Tan, X. H.; Stephenson, T. J.; King'ondu, C. K.; Holt, C. M. B.; Olsen, B. C.; Tak, J. K.; Harfield, D.; Anyia, A. O.; Mitlin, D. Interconnected Carbon Nanosheets Derived from Hemp for Ultrafast Supercapacitors with High Energy. *ACS Nano* **2013**, *7*, 5131−5141.
(13) Hu, Z.; Srinivasan, M. P. Mesoporous High-Surface-Area Activated Carbon. *Microporous Mesoporous Mater.* **2001**, *43*, 267−275.
(14) Wang, D. W.; Li, F.; Liu, M.; Lu, G. Q.; Cheng, H. M. 3D Aperiodic Hierarchical Porous Graphitic Carbon Material for High-Rate Electrochemical Capacitive Energy Storage. *Angew. Chem., Int. Ed.* **2008**, *47*, 373−376.
(15) Wang, G.; Wang, H.; Lu, X.; Ling, Y.; Yu, M.; Zhai, T.; Tong, Y.; Li, Y. Solid-State Supercapacitor Based on Activated Carbon Cloths Exhibits Excellent Rate Capability. *Adv. Mater.* **2014**, *26*, 2676−2682.
(16) Zhong, J.; Yang, Z.; Mukherjee, R.; Varghese Thomas, A.; Zhu, K.; Sun, P. Z.; Lian, J.; Zhu, H. W.; Koratkar, N. Carbon Nanotube Sponges as Conductive Networks for Supercapacitor Devices. *Nano Energy* **2013**, *2*, 1025−1030.
(17) Zhu, S.; Li, J.; Ma, L.; Guo, L.; Li, Q.; He, C.; Liu, E.; He, F.; Shi, C.; Zhao, N. Three-Dimensional Network of N-Doped Carbon Ultrathin Nanosheets with Closely Packed Mesopores: Controllable Synthesis and Application in Electrochemical Energy Storage. *ACS Appl. Mater. Interfaces* **2016**, *8*, 11720−11728.
(18) Zhang, L.; You, T.; Zhou, T.; Zhou, X.; Xu, F. Interconnected Hierarchical Porous Carbon from Lignin-Derived Byproducts of Bioethanol Production for Ultra-High Performance Supercapacitors. *ACS Appl. Mater. Interfaces* **2016**, *8*, 13918−13925.
(19) Yu, J.; Lu, W.; Pei, S.; Gong, K.; Wang, L.; Meng, L.; Huang, Y.; Smith, J. P.; Booksh, K. S.; Li, Q.; Byun, J.-H.; Oh, Y.; Yan, Y.; Chou, T.-W. Omnidirectionally Stretchable High-Performance Supercapacitor Based on Isotropic Buckled Carbon Nanotube Films. *ACS Nano* **2016**, *10*, 5204−5211.
(20) Wu, C.; Yang, S.; Cai, J.; Zhang, Q.; Zhu, Y.; Zhang, K. Activated Microporous Carbon Derived from Almond Shells for High Energy Density Asymmetric Supercapacitors. *ACS Appl. Mater. Interfaces* **2016**, *8*, 15288−15296.
(21) Ouyang, A.; Cao, A.; Hu, S.; Li, Y.; Xu, R.; Wei, J.; Zhu, H.; Wu, D. Polymer-Coated Graphene Aerogel Beads and Supercapacitor Application. *ACS Appl. Mater. Interfaces* **2016**, *8*, 11179−11187.
(22) Zhang, L. L.; Zhao, X. S. Carbon-Based Materials as Supercapacitor Electrodes. *Chem. Soc. Rev.* **2009**, *38*, 2520−2531.
(23) Liu, C.; Li, F.; Ma, L. P.; Cheng, H. M. Adv. Mater.for Energy Storage. *Adv. Mater.* **2010**, *22*, E28−E62.
(24) Béguin, F.; Presser, V.; Balducci, A.; Frackowiak, E. Supercapacitors: Carbons and Electrolytes for Advanced Supercapacitors (Adv. Mater. 14/2014). *Adv. Mater.* **2014**, *26*, 2283−2283.
(25) Wu, Z.-S.; Parvez, K.; Winter, A.; Vieker, H.; Liu, X.; Han, S.; Turchanin, A.; Feng, X.; Müllen, K. Layer-by-layer Assembled Heteroatom-Doped Graphene Films with Ultrahigh Volumetric Capacitance and Rate Capability for Micro-Supercapacitors. *Adv. Mater.* **2014**, *26*, 4552−4558.
(26) Soleimani, M.; Kaghazchi, T. Agricultural Waste Conversion to Activated Carbon by Chemical Activation with Phosphoric Acid. *Chem. Eng. Technol.* **2007**, *30*, 649−654.
(27) Liou, T. H. Development of Mesoporous Structure and High Adsorption Capacity of Biomass-Based Activated Carbon by Phosphoric Acid and Zinc Chloride Activation. *Chem. Eng. J.* **2010**, *158*, 129−142.
(28) Wang, R. T.; Wang, P. Y.; Yan, X. B.; Lang, J. W.; Peng, C.; Xue, Q. J. Promising Porous Carbon Derived from Celtuce Leaves with Outstanding Supercapacitance and CO2 Capture Performance. *ACS Appl. Mater. Interfaces* **2012**, *4*, 5800−5806.
(29) Song, X. L.; Zhang, Y.; Chang, C. M. Novel Method for Preparing Activated Carbons with High Specific Surface Area from Rice Husk. *Ind. Eng. Chem. Res.* **2012**, *51*, 15075−15081.
(30) Cai, J.; Niu, H.; Li, Z.; Du, Y.; Cizek, P.; Xie, Z.; Xiong, H.; Lin, T. High-Performance Supercapacitor Electrode Materials from Cellulose-Derived Carbon Nanofibers. *ACS Appl. Mater. Interfaces* **2015**, *7*, 14946−14953.
(31) Wei, X.; Wan, S.; Jiang, X.; Wang, Z.; Gao, S. Peanut-Shell-like Porous Carbon from Nitrogen-Containing Poly-N-phenylethanolamine for High-Performance Supercapacitor. *ACS Appl. Mater. Interfaces* **2015**, *7*, 22238−22245.
(32) Olivares-Marin, M.; Fernandez-Gonzalez, C.; Macias-Garcia, A.; Gomez-Serrano, V. Porous Structure of Activated Carbon Prepared from Cherry Stones by Chemical Activation with Phosphoric acid. *Energy Fuels* **2007**, *21*, 2942−2949.
(33) Gryglewicz, G.; Machnikowski, J.; Lorenc-Grabowska, E.; Lota, G.; Frackowiak, E. Effect of Pore Size Distribution of Coal-Based Activated Carbons on Double Layer Capacitance. *Electrochim. Acta* **2005**, *50*, 1197−1206.
(34) Wang, D. W.; Li, F.; Fang, H. T.; Liu, M.; Lu, G. Q.; Cheng, H. M. Effect of Pore Packing Defects in 2-D Ordered Mesoporous Carbons on Ionic Transport. *J. Phys. Chem. B* **2006**, *110*, 8570−8575.
(35) Jiang, W.; Zhai, S.; Qian, Q.; Yuan, Y.; Karahan, H. E.; Wei, L.; Goh, K.; Ng, A. K.; Wei, J.; Chen, Y. Space-Confined Assembly of All-Carbon Hybrid Fibers for Capacitive Energy Storage: Realizing A Built-To-Order Concept for Micro-Supercapacitors. *Energy Environ. Sci.* **2016**, *9*, 611−622.
(36) Zhou, C.; Zhang, Y. W.; Li, Y. Y.; Liu, J. P. Construction of High-Capacitance 3D CoO@Polypyrrole Nanowire Array Electrode for Aqueous Asymmetric Supercapacitor. *Nano Lett.* **2013**, *13*, 2078−2085.
(37) Abouali, S.; Akbari Garakani, M.; Zhang, B.; Xu, Z.-L.; Kamali Heidari, E.; Huang, J.-q.; Huang, J.; Kim, J.-K. Electrospun Carbon Nanofibers with In Situ Encapsulated Co3O4 Nanoparticles as Electrodes for High-Performance Supercapacitors. *ACS Appl. Mater. Interfaces* **2015**, *7*, 13503−13511.
(38) Purushothaman, K. K.; Manohara Babu, I.; Sethuraman, B.; Muralidharan, G. Nanosheet-Assembled NiO Microstructures for High-Performance Supercapacitors. *ACS Appl. Mater. Interfaces* **2013**, *5*, 10767−10773.
(39) Chen, Y.; Qu, B.; Hu, L.; Xu, Z.; Li, Q.; Wang, T. High-Performance Supercapacitor and Lithium-Ion Battery Based on 3D Hierarchical NH4F-Induced Nickel Cobaltate Nanosheet-Nanowire

DOI: 10.1021/acsami.6b08328
ACS Appl. Mater. Interfaces 2017, 9, 4362−4373

Cluster Arrays as Self-Supported Electrodes. *Nanoscale* **2013**, *5*, 9812−9820.
(40) Su, Z.; Yang, C.; Xie, B.; Lin, Z.; Zhang, Z.; Liu, J.; Li, B.; Kang, F.; Wong, C. P. Scalable Fabrication of MnO2 Nanostructure Deposited on Free-standing Ni Nanocone Arrays for Ultrathin, Flexible, High-performance Microsupercapacitor. *Energy Environ. Sci.* **2014**, *7*, 2652−2659.
(41) Kim, M.; Kim, J. Redox Deposition of Birnessite-Type Manganese Oxide on Silicon Carbide Microspheres for Use as Supercapacitor Electrodes. *ACS Appl. Mater. Interfaces* **2014**, *6*, 9036−9045.
(42) Wu, M.-S.; Zheng, Y.-R.; Lin, G.-W. Three-Dimensional Carbon Nanotube Networks with Supported Nickel Oxide Nanonet for High-Performance Supercapacitors. *Chem. Commun.* **2014**, *50*, 8246−8248.
(43) Zhu, D.; Wang, Y.; Yuan, G.; Xia, H. High-Performance Supercapacitor Electrodes Based on Hierarchical Ti@MnO2 Nanowire Nrrays. *Chem. Commun.* **2014**, *50*, 2876−2878.
(44) Li, L.; Zhang, X.; Qiu, J. J.; Weeks, B. L.; Wang, S. R. Reduced Graphene Oxide-Linked Stacked Polymer Forests for High Energy-Density Supercapacitor. *Nano Energy* **2013**, *2*, 628−635.
(45) Liu, Q.; Nayfeh, O.; Nayfeh, M. H.; Yau, S. T. Flexible Supercapacitor Sheets Based on Hybrid Nanocomposite Materials. *Nano Energy* **2013**, *2*, 133−137.
(46) Jiang, H.; Sun, T.; Li, C. Z.; Ma, J. Peapod-Like Nickel@Mesoporous Carbon Core-Shell Nanowires: A Novel Electrode Material for Supercapacitors. *RSC Adv.* **2011**, *1*, 954−957.
(47) Wu, Z.-S.; Zhou, G.; Yin, L.-C.; Ren, W.; Li, F.; Cheng, H.-M. Graphene/Metal Oxide Composite Electrode Materials for Energy Storage. *Nano Energy* **2012**, *1*, 107−131.
(48) Pognon, G.; Cougnon, C.; Mayilukila, D.; Belanger, D. Catechol-Modified Activated Carbon Prepared by the Diazonium Chemistry for Application as Active Electrode Material in Electrochemical Capacitor. *ACS Appl. Mater. Interfaces* **2012**, *4*, 3788−3796.
(49) Senthilkumar, S. T.; Selvan, R. K.; Melo, J. S.; Sanjeeviraja, C. High Performance Solid-State Electric Double Layer Capacitor from Redox Mediated Gel Polymer Electrolyte and Renewable Tamarind Fruit Shell Derived Porous Carbon. *ACS Appl. Mater. Interfaces* **2013**, *5*, 10541−10550.
(50) Zhao, D.; Guo, X. Y.; Gao, Y.; Gao, F. An Electrochemical Capacitor Electrode Based on Porous Carbon Spheres Hybrided with Polyaniline and Nanoscale Ruthenium Oxide. *ACS Appl. Mater. Interfaces* **2012**, *4*, 5583−5589.
(51) Yang, Y. J.; Li, S. B.; Zhang, L. N.; Xu, J. H.; Yang, W. Y.; Jiang, Y. D. Vapor Phase Polymerization Deposition of Conducting Polymer/Graphene Nanocomposites as High Performance Electrode Materials. *ACS Appl. Mater. Interfaces* **2013**, *5*, 4350−4355.
(52) Zhao, Y. F.; Ran, W.; He, J.; Song, Y. F.; Zhang, C. M.; Xiong, D. B.; Gao, F. M.; Wu, J. S.; Xia, Y. Y. Oxygen-Rich Hierarchical Porous Carbon Derived from Artemia Cyst Shells with Superior Electrochemical Performance. *ACS Appl. Mater. Interfaces* **2015**, *7*, 1132−1139.
(53) Wang, N.; Liu, Q.; Kang, D.; Gu, J.; Zhang, W.; Zhang, D. Facile Self-Cross-Linking Synthesis of 3D Nanoporous Co3O4/Carbon Hybrid Electrode Materials for Supercapacitors. *ACS Appl. Mater. Interfaces* **2016**, *8*, 16035−16044.
(54) Wen, X.; Zhang, D.; Shi, L.; Yan, T.; Wang, H.; Zhang, J. Three-Dimensional Hierarchical Porous Carbon with a Bimodal Pore Arrangement for Capacitive Deionization. *J. Mater. Chem.* **2012**, *22*, 23835−23844.
(55) Wang, H.; Shi, L.; Yan, T.; Zhang, J.; Zhong, Q.; Zhang, D. Design of Graphene-Coated Hollow Mesoporous Carbon Spheres as High Performance Electrodes for Capacitive Deionization. *J. Mater. Chem. A* **2014**, *2*, 4739−4750.
(56) Zhang, Z. J.; Chen, X. Y. Nitrogen-Doped Nanoporous Carbon Materials Derived from Folic Acid: Simply Introducing Redox Additive of P-Phenylenediamine into KOH Electrolyte for greatly Improving the Supercapacitor Performance. *J. Electroanal. Chem.* **2016**, *764*, 45−55.
(57) Wang, Z.; Yan, T. T.; Fang, J. H.; Shi, L. Y.; Zhang, D. S. Nitrogen-Doped Porous Carbon Derived from a Bimetallic Metal-Organic Framework as highly Efficient Electrodes for Flow-Through Deionization Capacitors. *J. Mater. Chem. A* **2016**, *4*, 10858−10868.
(58) Salunkhe, R. R.; Young, C.; Tang, J.; Takei, T.; Ide, Y.; Kobayashi, N.; Yamauchi, Y. A High-Performance Supercapacitor Cell Based on ZIF-8-Derived Nanoporous Carbon using an Organic Electrolyte. *Chem. Commun.* **2016**, *52*, 4764−4767.
(59) Boukhalfa, S.; Gordon, D.; He, L.; Melnichenko, Y. B.; Nitta, N.; Magasinski, A.; Yushin, G. In Situ Small Angle Neutron Scattering Revealing Ion Sorption in Microporous Carbon Electrical Double Layer Capacitors. *ACS Nano* **2014**, *8*, 2495−2503.
(60) Szczurek, A.; Jurewicz, K.; Amaral-Labat, G.; Fierro, V.; Pizzi, A.; Celzard, A. Structure and Electrochemical Capacitance of Carbon Cryogels Derived from Phenol-Formaldehyde Resins. *Carbon* **2010**, *48*, 3874−3883.
(61) Mysyk, R.; Raymundo-Piñero, E.; Béguin, F. Saturation of Subnanometer Pores in an Electric Double-Layer Capacitor. *Electrochem. Commun.* **2009**, *11*, 554−556.
(62) Raymundo-Pinero, E.; Leroux, F.; Beguin, F. A High-Performance Carbon for Supercapacitors Obtained by Carbonization of a Seaweed Biopolymer. *Adv. Mater.* **2006**, *18*, 1877−1882.
(63) Candelaria, S. L.; Shao, Y.; Zhou, W.; Li, X.; Xiao, J.; Zhang, J.-G.; Wang, Y.; Liu, J.; Li, J.; Cao, G. Nanostructured Carbon for Energy Storage and Conversion. *Nano Energy* **2012**, *1*, 195−220.
(64) Patil, P. D.; Gude, V. G.; Mannarswamy, A.; Cooke, P.; Nirmalakhandan, N.; Lammers, P.; Deng, S. G. Comparison of Direct Transesterification of Algal Biomass under Supercritical Methanol and Microwave Irradiation Conditions. *Fuel* **2012**, *97*, 822−831.
(65) Brousse, T.; Bélanger, D.; Long, J. W. To Be or Not To Be Pseudocapacitive? *J. Electrochem. Soc.* **2015**, *162*, A5185−A5189.
(66) Barranco, V.; Lillo-Rodenas, M. A.; Linares-Solano, A.; Oya, A.; Pico, F.; Ibanez, J.; Agullo-Rueda, F.; Amarilla, J. M.; Rojo, J. M. Amorphous Carbon Nanofibers and Their Activated Carbon Nanofibers as Supercapacitor Electrodes. *J. Phys. Chem. C* **2010**, *114*, 10302−10307.
(67) Aldama, I.; Barranco, V.; Centeno, T. A.; Ibanez, J.; Rojo, J. M. Composite Electrodes Made from Carbon Cloth as Supercapacitor Material and Manganese and Cobalt Oxide as Battery One. *J. Electrochem. Soc.* **2016**, *163*, A758−A765.
(68) Zhu, Y.; Cui, H.; Meng, X.; Zheng, J.; Yang, P.; Li, L.; Wang, Z.; Jia, S.; Zhu, Z. Chlorine-Induced In Situ Regulation to Synthesize Graphene Frameworks with Large Specific Area for Excellent Supercapacitor Performance. *ACS Appl. Mater. Interfaces* **2016**, *8*, 6481−6487.
(69) Phattharasupakun, N.; Wutthiprom, J.; Suksomboon, M.; Chiochan, P.; Kalasina, S.; Suktha, P.; Sawangphruk, M. Turning Conductive Carbon Nanospheres to Nanosheets for High-Performance Supercapacitors of MnO2 Nanorods. *Chem. Commun.* **2016**, *52*, 2585−2588.
(70) Peng, R.; Wu, N.; Zheng, Y.; Huang, Y.; Luo, Y.; Yu, P.; Zhuang, L. Large-Scale Synthesis of Metal-Ion-Doped Manganese Dioxide for Enhanced Electrochemical Performance. *ACS Appl. Mater. Interfaces* **2016**, *8*, 8474−8480.
(71) Ding, Y.; Bai, W.; Sun, J.; Wu, Y.; Memon, M. A.; Wang, C.; Liu, C.; Huang, Y.; Geng, J. Cellulose Tailored Anatase TiO2 Nanospindles in Three-Dimensional Graphene Composites for High-Performance Supercapacitors. *ACS Appl. Mater. Interfaces* **2016**, *8*, 12165−12175.
(72) Moosavifard, S. E.; El-Kady, M. F.; Rahmanifar, M. S.; Kaner, R. B.; Mousavi, M. F. Designing 3D Highly Ordered Nanoporous CuO Electrodes for High-Performance Asymmetric Supercapacitors. *ACS Appl. Mater. Interfaces* **2015**, *7*, 4851−4860.
(73) Huang, M.; Zhang, Y. X.; Li, F.; Zhang, L. L.; Wen, Z. Y.; Liu, Q. Facile Synthesis of Hierarchical Co3O4@MnO2 Core-Shell Arrays on Ni Foam for Asymmetric Supercapacitors. *J. Power Sources* **2014**, *252*, 98−106.
(74) Wang, X.; Liu, J. Y.; Wang, Y. Y.; Zhao, C. M.; Zheng, W. T. Ni(OH)(2) Nanoflakes Electrodeposited on Ni Foam-Supported

DOI: 10.1021/acsami.6b08328
ACS Appl. Mater. Interfaces 2017, 9, 4362−4373

Vertically Oriented Graphene Nanosheets for Application in Asymmetric Supercapacitors. *Mater. Res. Bull.* **2014**, *52*, 89−95.
(75) Wang, X.; Sumboja, A.; Lin, M. F.; Yan, J.; Lee, P. S. Enhancing Electrochemical Reaction Sites in Nickel-Cobalt Layered Double Hydroxides on Zinc Tin Oxide Nanowires: A Hybrid Material for an Asymmetric Supercapacitor Device. *Nanoscale* **2012**, *4*, 7266−7272.

DOI: 10.1021/acsami.6b08328
ACS Appl. Mater. Interfaces 2017, 9, 4362−4373